Materials Research Bulletin 65 (2015) 163–168

Contents lists available at ScienceDirect

Materials Research Bulletin

journal homepage: www.elsevier.com/locate/matresbu

Amorphous iron–chromium oxide nanoparticles with long-term stability

Mihail Iacob [a,b], Maria Cazacu [a,*], Constantin Turta [b], Florica Doroftei [a], Martin Botko [c], Erik Čižmár [c], Adriana Zeleňáková [c], Alexander Feher [c]

[a] "Petru Poni" Institute of Macromolecular Chemistry, Iasi 700487, Romania
[b] Institute of Chemistry of ASM, Academiei str. 3, Chisinau 2028, Republic of Moldova
[c] Institute of Physics, Faculty of Science, P.J. Šafárik University, Park Angelinum 9, SK-04154 Košice, Slovakia

ARTICLE INFO

Article history:
Received 24 June 2014
Received in revised form 3 November 2014
Accepted 25 January 2015
Available online 28 January 2015

Keywords:
Iron–chromium oxide
Amorphous
Nanoparticles
Morphology
Magnetic properties

ABSTRACT

Iron–chromium nanoparticles (NPs) were obtained through the thermal decomposition of μ_3-oxo heterotrinuclear $\{FeCr_2O\}$ acetate in the presence of sunflower oil and dodecylamine (DA) as surfactants. The average diameter of the NPs was 3.5 nm, as estimated on the basis of transmission electron microscopy and atomic force microscopy images. Both techniques revealed the formation of roughly approximated spheres with some irregularities and agglomerations in larger spherical assemblies of 50–100 nm. In hexane, NPs with diameters in the 2.33–4.85 nm range are individually dispersed, as emphasized by dynamic light scattering measurements. The amorphous nature of the product was emphasized by X-ray powder diffraction. The study of the magnetic properties shows the presence of superparamagnetic state of iron–chromium oxide NPs and the diamagnetic contribution from DA layer forming a shell of NPs.

1. Introduction

Amorphous iron-oxide nanoparticles (NPs) are of high interest for catalysis as well as sensors, owing to their large surface area [1–4]. They can be synthesized by various methods such as electrochemical [5] or sonochemical techniques [2,6–8], microwave heating [9], hydrothermal treatment [10], thermal decomposition in the solid state or in solution [11], and in the presence or absence of some organic components, for example, in a mixture of polyethyleneglycol and urea [8] or with citric acid as a fuel [11]. In general, the used procedures started from iron salts (e.g., chlorides [10], nitrates [11], or chloride–nitrate [8]). Amorphous phase formation requires special conditions such as a high cooling rate, the sonochemical technique being one that could permit the creation of such conditions [4,12]. But as is known [4], the amorphous state is metastable and changes to the crystalline state through a crystallization process, during which long-range order can be formed and the physical and chemical properties of materials change accordingly, thus affecting the stability of the materials under ambient conditions. The crystallization process depends on temperature and time. Therefore, aging effects can be prevented by a material synthesis procedure and by keeping it at a low temperature. Nguyen et al. [4,8] introduced different amounts of chromium into amorphous iron oxide NPs to slow down the aging effect. Based on thermal analysis, it has been showed that the chromium presence leads to increasing in activation energy of the phase transition, which could slow the ageing effect of the amorphous state during practical use [8]. Pt supported on Fe–Cr mixed oxides, prepared by the solid thermal decomposition reaction, proved to be an effective catalyst. By adding chromium compounds, Pt dispersion was improved and, as a result, the catalytic performance increased. Moreover, the addition of Cr_2O_3 to Fe–Cr mixed oxides increased their Brunauer–Emmett–Teller (BET) surface area, but also the amount of magnetite in the composition [11]. $(Fe,Cr)_2O_3$ systems proved to have other applications as pigments as well as mineralogical, magnetic, abrasive, sensor, and refractory materials in the ceramic industry [13].

Iron–chromium oxide NPs, both in crystalline [10,11,14] and amorphous [4,8] states, were obtained using the same procedures as used to obtain single iron oxide, such as ultrasonic radiation [4,8], hydrothermal methods [10], and thermal decomposition [11,14], using physical mixtures of salts as metals sources. According to previously published reports [4,8], amorphous iron–chromium oxide NPs have been prepared using iron chloride and chromium nitrate in different molar ratios as precursors.

* Corresponding author. Tel.: +40 232217454; fax: +40 232211299.
E-mail address: mcazacu@icmpp.ro (M. Cazacu).

http://dx.doi.org/10.1016/j.materresbull.2015.01.055
0025-5408/

However, in the case of amorphous materials, a precise determination of the two nuclei cannot be determined by X-ray diffraction, thus their characterization is quite difficult. In our recent work [14], we reported obtaining crystalline iron–chromium oxide NPs starting from a mixed metal complex with a pre-established iron/chromium ratio.

In this paper, using the same metal source (iron–chromium acetate clusters, $[FeCr_2O(CH_3COO)_6(H_2O)_3]\cdot NO_3$) and the same procedure (thermal decomposition) in the presence of dodecylamine (DA) and trichloroacetic acid (TCAA), but replacing oleic acid with a cheap and easily accessible surfactant (sunflower oil, SO), which is added in a high excess without any special conditions (cooling for example), we obtained amorphous and well-defined iron–chromium oxide, which exhibited long-term stability. The formation of the NPs was demonstrated by transmission electron microscopy (TEM), atomic force microscopy (AFM), and dynamic light scattering (DLS). The amorphous nature was proven by X-ray powder diffraction (XRPD), whereas the co-existence of iron and chromium was verified by energy-dispersive X-ray (EDX) spectroscopy. Magnetic measurements performed in the 1.8–300 K temperature range and in magnetic fields up to 50 kOe confirmed presence of superparamagnetic state. The existence of an organic surface layer on NPs is responsible for the diamagnetic contribution to the total magnetization of the system.

2. Experimental

2.1. Materials

Heteronuclear iron–chromium acetate (also known as $[FeCr_2O(CH_3COO)_6(H_2O)_3]\cdot NO_3$), {$FeCr_2O$}, and ICA), with a Cr/Fe molar ratio of 2:1 (as determined by EDX; Fig. 1S) [14], was prepared following a previously reported procedure [15], using Fe$(NO_3)_3\cdot 9H_2O$ (Sigma–Aldrich) and Cr$(NO_3)_3\cdot 9H_2O$ (Sigma–Aldrich) in a 1:2 molar ratio and calcium acetate monohydrate, [Ca$(CH_3COO)_2\cdot H_2O$] (Sigma–Aldrich), glacial acetic acid (chemical company), and distilled water. TCAA (CCl_3COOH; Fluka), DA [$CH_3(CH_2)_{11}NH_2$; Fluka], SO ("Sorica" brand by Argus S.A. Constanta, Romania), hexane, and ethanol (chemical company) were used as received.

2.2. Equipment

An EDX system available on a Quanta 200 environmental scanning electron microscope (ESEM) was used for qualitative analysis and elemental mapping.

The infrared spectra were registered on a Bruker Vertex 70 FT-IR instrument in transmission mode, in the 300–4000 cm^{-1} range (resolution 2 cm^{-1}, 32 scans), at ambient temperature.

TEM investigations were carried out with a Hitachi High-Tech HT7700 transmission electron microscope operated at a 100 kV accelerating voltage in high-contrast mode. The samples were prepared on carbon-coated copper grids with 200-mesh size. Microdroplets of the NPs dispersed in hexane (0.1%) were placed on the grids, and then the solvent was removed under vacuum.

Wide-angle X-ray diffraction (WAXRD) was performed on a Bruker-AXS D8 ADVANCE diffractometer, with a Bragg–Brentano para-focusing goniometer. Scans were recorded in step mode using Ni-filtered Cu Kα radiation (λ = 0.1541 nm). The working conditions were 40 kV and 30 mA tube power. The Bruker computer software packages Eva 11 and Topaz 3.1 were used to plot and process the data.

Thermogravimetric analysis (TGA) was performed on a Mettler Toledo TGA-SDTA851e type derivatograph (thermogravimetric analyzer) under a flow of nitrogen (20 mL/min), within 25–800 °C at 10 °C min^{-1} for samples of 2–5 mg each. Alumina crucibles (70 μL) were used as sample holders. Each experiment was repeated three times and exhibited a good reproducibility. The data were processed using Mettler Toledo STAR software.

Magnetic measurements were performed on powdered samples placed inside inert gelatin capsules using a Quantum Design SQUID magnetometer. The raw data were corrected for the background signal resulting from the gelatin capsule, which was obtained from a separate measurement. The magnetic moment was measured in a direct-current (dc) magnetic field in the 2–300 K temperature range within zero-field-cooled (ZFC) and field-cooled (FC) regimes.

AFM measurements were made on a SPM Solver Pro-M platform (NT-MDT, Russia) instrument in air, using semi-contact mode with a rectangular NSG10/Au cantilever and a nominal elasticity constant of $K_N = 11.5$ Nm^{-1}. Drops of the particle dispersion were placed on glass slides and slowly dried at room temperature prior to analysis.

The average particle-size diameter and distribution (polydispersity index) were determined by DLS on a Malvern Zetasizer NS (Malvern Instruments, UK) instrument, which uses noninvasive backscatter detection (NIBS) (173°) and a laser wavelength of 633 nm. The particles were dispersed in hexane. The autocorrelation signal was analyzed by the cumulant method, giving the *z*-average diameter of the particles and the polydispersity index according to ISO13321, part 8.

2.3. Preparation of iron–chromium oxide NPs

A mixture of iron–chromium acetate (0.4 g, 0.63 mmol), dodecylamine (2 g, 10.79 mmol), trichloroacetic acid (2.5 g, 15 mmol) and sunflower oil (4 mL) was heated stepwise in a three-necked flask equipped with a condenser, thermometer, and heating mantle until a temperature of 320 °C was reached; the

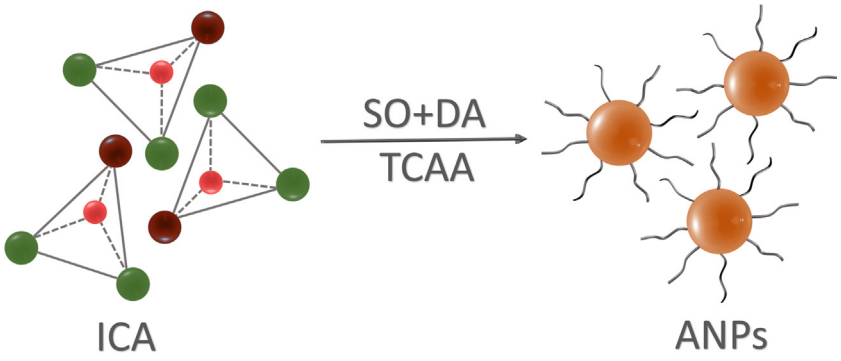

Scheme 1. A graphical representation of the process of forming the amorphous NPs (ANPs).

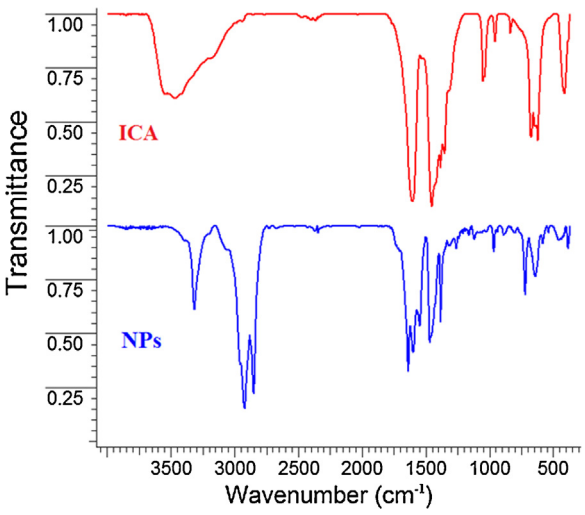

Fig. 1. FT-IR spectra for ANPs and ICA.

mixture was maintained at this temperature for 1 h before it was gradually cooled to room temperature, diluted with 40 mL hexane, and filtered. The filtrate was centrifuged for 15 min at 6000 rpm. The separated solid was washed three times with ethanol and dried, yielding a black powder. FT-IR (KBr), ν, cm^{-1}: 384 (w), 455 (vw), 538 (vw), 581 (vw), 640 (w), 667 (w), 719 (m), 804 (vw), 889 (vw), 964 (w), 1119 (vw), 1240 (vw), 1261 (vw), 1385 (m), 1468 (s), 1499 (vw), 1547(m), 1599 (s), 1638 (s), 1701 (w), 1719 (w), 1734 (w), 2851 (vs), 2920(vs), 2956 (s), 3316 (m). The Cr/Fe atomic ratio estimated through EDX was 1.754 (Fig. 2S).

3. Results and discussion

A mixture containing ICA as the oxide precursor as well as SO and DA as surfactants and TCAA as a solvent was heated to 320 °C, at which a thermal decomposition process occurred with the formation of iron–chromium oxide NPs (Scheme 1).

In fact, at such a temperature, according to previous reports [16,17], different processes can take place, such as progressive ligand substitution (in which acetic acid is replaced by unsaturated acids, mostly oleic and linoleic acids that are present in SO), decomposition of metal alkenic carboxylates (with formation of oxide NPs), and stabilization of the NPs by DA and alkenic carboxylic acids. By using mixed ICA clusters as precursors, we have a pre-established ratio between the two metals in the resulting oxide.

The infrared spectrum of the NPs, as compared with that for ICA, is presented in Fig. 1. By examining Fig. 1, a shift of the

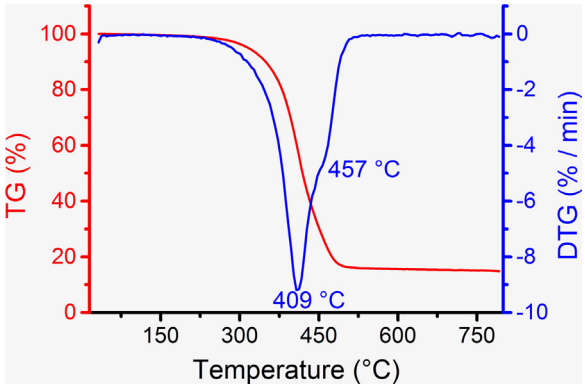

Fig. 2. TGA and DTGA curves for organic-coated ANPs sample.

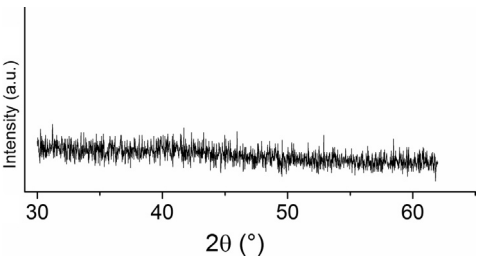

Fig. 3. WAXRD spectrum for the obtained NPs registered after two years.

carboxylate bands (1547 and 1468 cm^{-1}) can be seen in the NPs compared with the starting acetate (1605 and 1454 cm^{-1}, respectively), suggesting the replacement of the acetate ligand with unsaturated acids from the SO [18]. The shoulder at 3057 cm^{-1} (C—H from an alkenyl group) indicates the presence of unsaturation, which was retained, even though previous reports support the carrying out of chemical changes during thermal treatment [17]. The bands at 3316 and 1638 cm^{-1} indicate the presence of DA on the surface of the oxide NPs. The bands present in the 600–400 cm^{-1} range of the FTIR spectrum of the NPs (Fig. 1) are characteristic of metal oxides. The band at 538 cm^{-1} is assigned to the Cr—O vibration, whereas a wider band centered at 640 cm^{-1} could be assigned to Fe—O vibrations, as indicated in previously published reports [19]. Many other bands that are characteristic of the organic compounds used in the synthesis are also present. The bands at 2957, 2870 (shoulder) and 2920, as well as 2851 cm^{-1} are assigned to asymmetrical and symmetrical stretching vibrations as well as $\nu_{as,s}$(C—H) from CH_3 and CH_2 groups, respectively [20] (DA and fatty acids).

The TGA results (Fig. 2 and Fig. 3S) reveal good thermal stability of the obtained NPs. These NPs begin to lose mass at around 318 °C, and the process mainly occurs in two close steps with maxima (from derivative TGA; DTGA) at 409 and 457 °C, at which evaporation/decomposition of the surfactants, which form the protective shell of the NPs, could occur. The mass changes during these processes were 54 and 29 wt%, respectively. The residual mass at the end of the analysis (at 750 °C) was 17 wt%. The high mass loss (around 83 wt%) indicates a high content of organic component as coatings for the metal oxide NPs.

The WAXRD pattern of the investigated sample is presented in Fig. 3, which was taken two years after the production of the NPs. It does not contain any peaks; this indicates the presence of only an amorphous phase in the product and highlights its stability over a prolonged time. One explanation for this could be that it is has a high organic content.

In Fig. 4, the TEM images, electron diffraction pattern, and corresponding particles size histogram are presented. The geometry of the particles may be roughly approximated as spheres

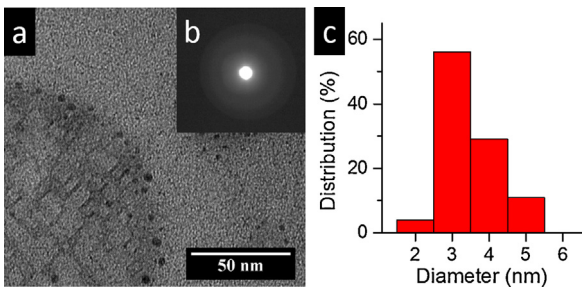

Fig. 4. TEM image (a), electron diffraction pattern (b), and histogram of the NPs according to the TEM image (c).

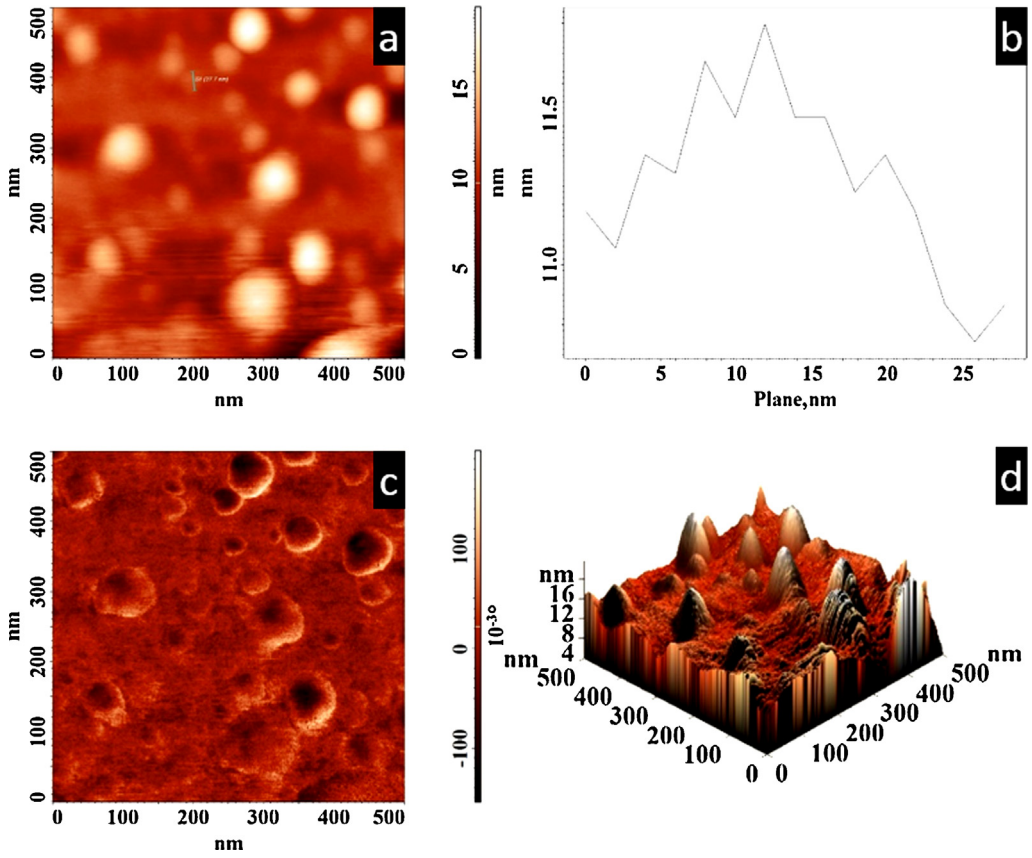

Fig. 5. AFM results for the NPs: 2D height image (a), cross-surface profile taken along a structural formation of agglomerated particles (b), phase image (c), and 3D height image (d).

with some irregularities. The images were processed with ImageJ 3.0 software in order to obtain the derived histogram (Fig. 4c). The analysis demonstrated that the particles size was in the 2–5 nm range; thus, the main diameter of 3.5 ± 1.5 nm was found. These are agglomerated into larger spherical assembles on the order of 50–100 nm.

The AFM images (Fig. 5) reveal the surface morphology of the NPs over a scanning area of $500 \times 500\ nm^2$. At first sight, in the 2D images, the presence of the agglomerates of different sizes can be seen, whereas the 3D images reveal the contour of the individual NPs better and allow us to estimate their size in the same range as observed by TEM.

The size and dispersion of the NPs were also measured by DLS. The size distribution of the particles in hexane is presented in Fig. 6. According to the DLS results, 34.3% of the particles have a diameter of 3.12 nm and the values of the particle diameter are distributed in the 2.33–4.85 nm range. Thus, although in the solid state the NPs are agglomerated, in solution they seem to be dispersed at the individual NP level.

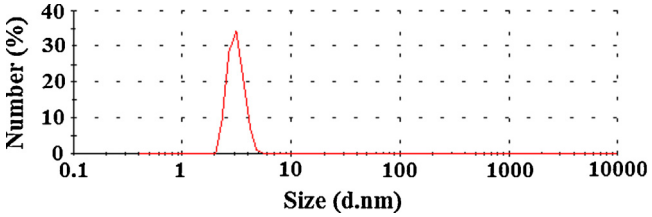

Fig. 6. The size distribution of the particles (in terms of the number of individual particles) in hexane solution versus aggregate sizes in hexane solution as was evidenced by DLS.

The temperature dependence of dc magnetization, measured in both ZFC and FC mode, exhibits deviation from the typical paramagnetic behavior (see Figs. 7 and 8). The ZFC and FC magnetization curves measured in a low external magnetic field of 10 Oe exhibit the high irreversibility, whereas the ZFC curve shows a broad maximum around a temperature of 200 K. With increasing external magnetic field from 10 to 100 Oe, the maximum flattens and is not observable at 100 Oe. This could suggest the presence of a superparamagnetic state, but, in comparison with other superparamagnetic systems [22–24], the blocking temperature is not clearly evident (Fig. 8) because of the small particle size and low concentration of magnetic atoms.

It should be noted that the maximum around 50 K, in both thermomagnetic curves, is associated with the paramagnetic–antiferromagnetic transition of solid oxygen and has no further effect on the magnetic properties [28].

The dependence of the magnetization of the measured sample on the magnetic field at different temperatures is shown in Fig. 9. The magnetization curve measured at 300 K (blue squares) shows a dominant diamagnetic behavior in higher applied fields, which complies with the results of infrared spectroscopy, where the FT-IR spectrum confirms the presence of DA on the surface of the oxide NPs. The saturation magnetization increases due to the thermal effect proportional to k_BT with decrease of the temperature (at 2 and 10 K) and the contribution of superparamagnetic particles to the total magnetic moment is higher. Magnetization curves at 10 K (red triangles) and 2 K (black circles) are reversible and no hysteresis was observed. We calculated the magnetic moment of the chromium–ferric oxide NPs from experimental data at 10 and

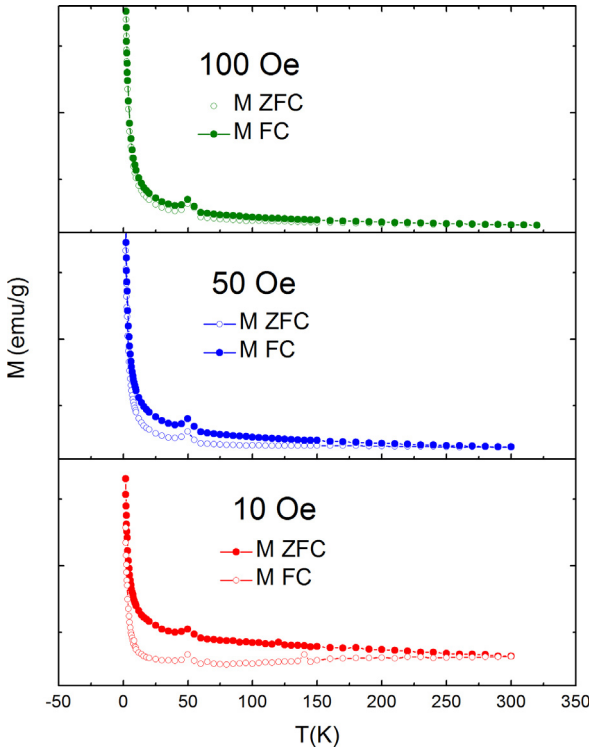

Fig. 7. The influence of the external magnetic field of 10, 50, and 100 Oe on the shape of the ZFC and FC thermomagnetic curves.

2 K using a simple Langevin function [22]. The small magnetic moment of the particles estimated using this procedure (around $m_P \sim 5.6 \times 10^{-3}\ \mu_B$) also confirms a small concentration of magnetic atoms in the studied NPs.

The magnetization and magnetic susceptibility in the ferrite nanoparticles strongly depends on the size of the particles and the preparation route [25]. For example, Kundu et al. [26] prepared $ZnFe_2O_4$ nanoparticles of size 13 nm using co-precipitation technique, using urea hydrolysis, and reported magnetization of about 21 emu/g at applied field of 10 kOe. Shenoy et al. [27] prepared $ZnFe_2O_4$ nanosized particles using co-precipitation technique followed by ball milling and for 9 nm particles found saturation magnetization around 7.5 emu/g. Pandey [25] prepared nanosized $CrFe_2O_4$ particles of different sizes (6, 7, 11, 12 and

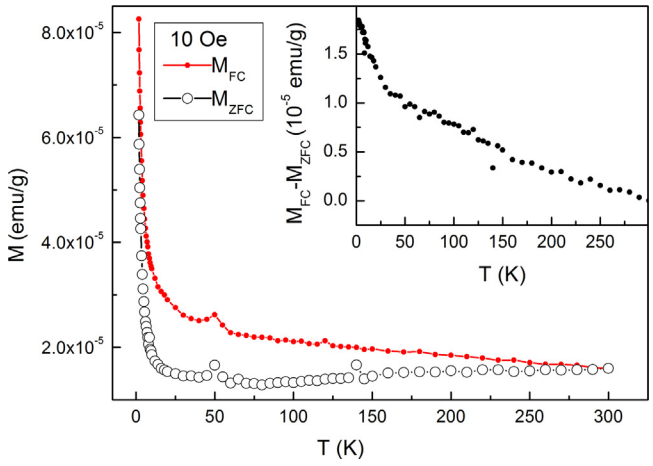

Fig. 8. Temperature dependence of the magnetization measured in the ZFC and FC regimes in a magnetic field of 10 Oe. The inset shows the difference between FC and ZFC magnetization.

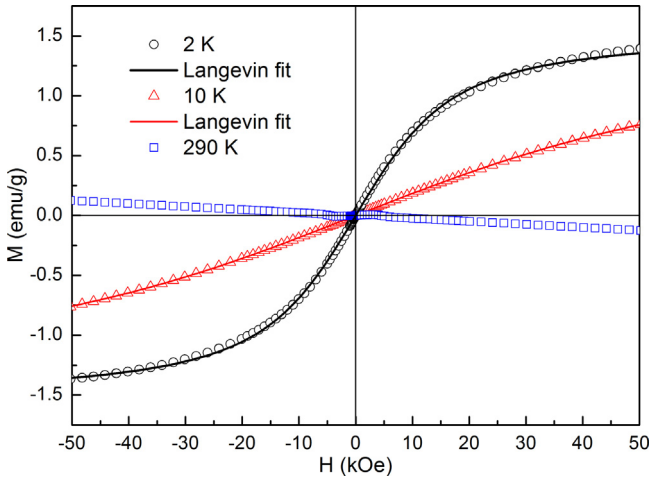

Fig. 9. Field dependence of magnetization at different temperatures of 2, 10, and 300 K with the corresponding Langevin fit of the experimental data, calculated according to Ref. [22]. (For interpretation of the references to color in this text, the reader is referred to the web version of this article.)

35 nm) using citrate precursor route and found that for small paramagnetic particles of 6–12 nm the saturation magnetization is very small (around 4 emu/g) and strongly increases up to 11 emu/g for 35 nm particles. The values of the magnetic moment and the saturation magnetization in our system correspond to the small size of chromium ferrite particles (3.5 nm) and to the high dilution of nanoparticles in amorphous aggregates of the organic-coating layer that creates 83 wt% of the sample.

4. Conclusion

μ_3-Oxo heterotrinuclear $\{FeCr_2O\}$ acetate (ICA) was used as an oxide precursor together with sunflower oil (SO) and dodecylamine (DA) as surfactants and trichloroacetic acid (TCAA) as a solvent, which were heated together, resulting in iron–chromium oxide NPs. During this treatment, the decomposition of metal carboxylates occurs, with the formation of mixed-oxide NPs and a stabilization of the NPs by DA and fatty acids from SO, which also act as a shell. A high organic-coating content of 83 wt% was estimated, based on thermogravimetric analysis. The diameter of the NPs was estimated on the basis of TEM, AFM, and DLS measurements to be only a few nanometers. Although in solid state these showed agglomerates, in liquid medium (hexane), they were dispersed as individual particles. The X-ray diffraction pattern indicated a completely amorphous product, and this state was maintained even after two years. The high excess of SO used as the surfactant favored the formation and stabilization of the amorphous state. Owing to the high intrinsic surface area conferred by this phase state, the obtained iron–chromium oxide NPs could be of interest for catalysis. Magnetic measurements demonstrated the presence of a superparamagnetic state in the studied system as well as the co-existence of a diamagnetic contribution from the organic-surface layer of NPs.

Acknowledgements

This work was supported by a grant of the Ministry of National Education,CNCS – UEFISCDI, project number PN-II-ID-PCE-2012-4-0261, contract no. 53/2.09.2013; by the Slovak Research and Development Agency under contract no. APVV-0132-11; and by the Slovak Grant Agency, contract no. VEGA 1/0145/13. Support by the COST Action (MP1003) "European Scientific Network for Artificial Muscles (ESNAM)", through Short-Term Scientific Mission COST-

STSM-MP1003-16691 which benefited Mihail Iacob is also gratefully acknowledged.

Appendix A. Supplementary data

Supplementary data associated with this article can be found, in the online version, at http://dx.doi.org/10.1016/j.materresbull.2015.01.055.

References

[1] N. Perkas, Y. Koltypin, O. Palchik, A. Gedanken, S. Chandrasekaran, Oxidation of cyclohexane with nanostructured amorphous catalysts under mild conditions, Appl. Catal. A Gen. 209 (2001) 125.
[2] D.N. Srivastava, N. Perkas, A. Gedanken, I. Felner, Sonochemical synthesis of mesoporous iron oxide and accounts of its magnetic and catalytic properties, J. Phys. Chem. B 106 (2002) 1878.
[3] G. Neri, A. Bonavita, C. Milone, A. Pistone, S. Galvagno, Gold-promoted Li–Fe_2O_3 thin films for humidity sensors, Sens. Actuators B-Chem. 92 (2003) 326.
[4] D.P. Nguyen, Q.T. Tran, X.S. Trinh, T.C. Hoang, H.N. Nguyen, H.H. Nguyen, Crystallization and magnetic properties of amorphous iron–chromium oxide nanoparticles synthesized by sonochemistry, Adv. Nat. Sci. Nanosci. Nanotechnol. 3 (2012) 015017.
[5] C. Pascal, J.L. Pascal, F. Favier, M.L. Elidrissi Moubtassim, C. Payen, Electrochemical synthesis for the control of γ-Fe_2O_3 nanoparticle size, morphology, microstructure, and magnetic behavior, Chem. Mater. 11 (1999) 141.
[6] J. Pinkas, V. Reichlova, R. Zboril, Z. Moravec, P. Bezdicka, J. Matejkova, Sonochemical synthesis of amorphous nanoscopic iron(III) oxide from Fe $(acac)_3$, Ultrason. Sonochem. 15 (2008) 257.
[7] K.V.P.M. Shafi, A. Ulman, X. Yan, N.-L. Yang, C. Estournès, H. White, M. Rafailovich, Sonochemical synthesis of functionalized amorphous iron oxide nanoparticles, Langmuir 17 (2001) 5093.
[8] N.D. Phu, T.X. Sy, H.T. Cao, N.N. Dinh, L. van Thien, N.M. Hieu, N.H. Nam, N.H. Hai, Amorphous iron–chromium oxide nanoparticles prepared by sonochemistry, J. Non. Cryst. Solids 358 (2012) 537.
[9] X. Liao, J. Zhu, W. Zhong, H.-Y. Chen, Synthesis of amorphous Fe_2O_3 nanoparticles by microwave irradiation, Mater. Lett. 50 (2001) 341.
[10] M. Sorescu, L. Diamandescu, D. Tarabasanu-Mihaila, S. Krupa, M. Feder, Iron and chromium mixed-oxide nanocomposites, Hyperfine Interact. 196 (2010) 359.
[11] X. Liu, K. Shen, Y. Wang, Y. Wang, Y. Guo, Y. Guo, Z. Yong, G. Lu, Preparation and catalytic properties of Pt supported Fe–Cr mixed oxide catalysts in the aqueous-phase reforming of ethylene glycol, Catal. Commun. 9 (2008) 2316.
[12] K.S. Suslick, S.-B. Choe, A.A. Cichowlas, M.W. Grinstaff, Sonochemical synthesis of amorphous iron, Nature 353 (1991) 414.
[13] V. Biondo, S.N. de Medeiros, A. Paesano, L. Ghivelder, B. Hallouche, J.B.M. da Cunha, Structural and Mossbauer characterization of the ball milled $Fe_x(Cr_2O_3)_{1-x}$, Solid State Sci. 11 (2009) 1444.
[14] M. Iacob, M. Cazacu, C. Racles, M. Ignat, V. Cozan, L. Sacarescu, D. Timpu, M. Kajňaková, M. Botko, A. Feher, C. Turta, Iron–chromium oxide nanoparticles self-assembling into smectic mesophases, RSC Adv. 4 (2014) 6293.
[15] T. Głowiak, M. Kubiak, T. Szymańska-Buzar, B. Jezowska-Trzebiatowska, Crystal and molecular structure of the trinuclear chromium(III) and iron(III) complex, $[Cr_2FeO(CH_3COO)_6(H_2O)_3]NO_3 \cdot CH_3COOH$, Acta Crystallogr., Sect. B: Struct. Crystallogr. Cryst. Chem. 33 (1977) 3106.
[16] A. Valor, E. Reguera, E. Torres-Garcı'a, S. Mendoza, F. Sanchez-Sinencio, Thermal decomposition of the calcium salts of several carboxylic acids, Thermochim. Acta 389 (2002) 133.
[17] W.W. Yu, J.C. Falkner, C.T. Yavuz, V.L. Colvin, Synthesis of monodisperse iron oxide nanocrystals by thermal decomposition of iron carboxylate salts, Chem. Commun. (Camb) (2004) 2306.
[18] A.L. Willis, N.J. Turro, S. O'Brien, Spectroscopic characterization of the surface of iron oxide nanocrystals, Chem. Mater. 17 (2005) 5970.
[19] J.E. Amonette, D. Rai, Identification of noncrystalline (Fe,Cr)$(OH)_3$ by infrared spectroscopy, Clays Clay Miner. 38 (1990) 129.
[20] K. Nakamoto, Infrared and Raman Spectra of Inorganic and Coordination Compounds, John Wiley & Sons, 1986.
[22] A. Zeleňáková, V. Zeleňák, Š. Michalík, J. Kováč, M.W. Meisel, Structural and magnetic properties of CoO–Pt core–shell nanoparticles, Phys. Rev. B 89 (2014) 104417.
[23] S. Bedanta, W. Kleemann, Supermagnetism, J. Phys. D: Appl. Phys. 42 (2009) 013001.
[24] S. Mørup, M.F. Hansen, C. Frandsen, Magnetic interactions between nanoparticles, Beilstein J. Nanotechnol. 1 (2010) 182.
[25] B. Pandey, Mössbauer and magnetization studies of nanosize chromium ferrite, Int. J. Eng. Sci. Technol. 2 (2010) 80.
[26] A. Kundu, C. Upadhyay, H.C. Verma, Magnetic properties of a partially inverted zinc ferrite synthesized by a new coprecipitation technique using urea, Phys. Lett. A 311 (2003) 410.
[27] S.D. Shenoy, P.A. Joy, M.R. Anantharaman, Effect of mechanical milling on the structural, magnetic and dielectric properties of coprecipitated ultrafine zinc ferrite, J. Magn. Magn. Mater. 269 (2004) 217.
[28] S. Gregory, Magnetic susceptibility of oxygen adsorbed on graphite, Phys. Rev. Lett. 40 (1978) 723.